

pubs.acs.org/JPCC Article

Solid-State Properties and Spectroscopic Analysis of Thin-Film TPBi

Jazmin Calimano, Feifei Li, Jan Florián, Dalice M. Piñero-Cruz, Thomas R. Fielitz, Russell J. Holmes, and Jacob W. Ciszek*



Cite This: J. Phys. Chem. C 2020, 124, 23716-23723



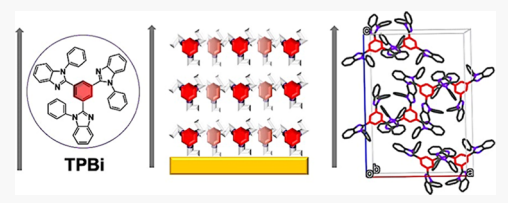
ACCESS

Metrics & More



Supporting Information

ABSTRACT: We characterized the prominent electron transport layer 2,2',2''-(1,3,5)-benzinetriyl)-tris(1-phenyl-1-H-benzimidazole) (TPBi) via single-crystal X-ray diffraction, grazing incidence X-ray diffraction (GIXRD), infrared reflection absorption spectroscopy (IRRAS), and quantum mechanical calculations. The crystals generated via vapor diffusion are of the orthorhombic space group *Pbca*, with a unit cell [$\mathbf{a} = 19.3935(2)$ $\mathbf{b} = 12.81750(10)$ $\mathbf{c} = 28.5610(3)$ Å] containing eight TPBi molecules, and screw axes and glide planes along all three



crystallographic axes. Thin-film analysis becomes viable with unit cell and symmetry data, and GIXRD measurements, which demonstrate that when the amorphous TPBi thin films are annealed, the molecules preferentially orient with the a-b crystallographic face exposed at the surface and with the central benzene rings oriented 29° from the surface normal. Changes in vibrational modes at the surface, studied via infrared reflection absorption spectroscopy (IRRAS), concur with the X-ray based assignments. A minor conformer of TPBi with C_3 symmetry was also identified via computational methods, appearing 0.95 kcal/mol higher in energy at the MP2/6-31G*//B3LYP/6-31G* level of theory. The combined structural insight allows fine-tuning of a device structure for organic light-emitting diodes (OLEDs) and organic photovoltaic applications.

■ INTRODUCTION

In modern OLED devices, the organic stack typically terminates in an electron transport layer (ETL), which serves as a conduit from the cathode to the emissive layer. These materials are expected to be multifunctional; they must have proper energy alignment, high optical transmittance ability, high thermal stability/glass transition temperatures, and high electron mobility.^{2,3} While many candidates have been developed over the years, only a handful play a significant role in devices today, including the titular TPBi (2,2',2"-(1,3,5benzinetriyl)-tris(1-phenyl-1-H-benzimidazole)). TPBi was first introduced as an ETL layer by Tang⁴ and displayed high electron mobility, high glass transition temperature, and propensity to reduce contact-based issues. 5-7 Additionally, its excellent properties mean it also finds use in other optoelectronic applications, including as a buffer layer in organic solar cells⁸ and as a host in emissive layers. Thus, the electronic properties of TPBi have been extensively studied.¹⁰⁻¹³

In contrast to its electronic properties, the characterization of TPBi's chemical and material properties is sparse. TPBi is generally understood to be deposited as an amorphous glass when thermally evaporated onto room temperature substrates, 14,15 which has the added advantage of reducing surface roughness leading to cleaner interfaces. It has also been shown that, despite depositing in an amorphous manner, the thin films can be annealed at temperatures above TPBi's glass transition temperature to impart some order. 14

The previous annealing experiment serves as an example of how limited characterization undermines research of these materials. In this experiment, XRD analysis of the thin film determined d_{hkl} spacing, but the lack of available crystal structure data prevented any meaningful interpretation. It was thus impossible to determine molecular orientation within the film. The lack of information extends well beyond and is at times glaring. Simple structural information, such as the orientation of the benzimidazole and phenyl rings, are unknown. The anisotropy of optical properties is undefined, and molecular packing structures are absent. This is glaring since these properties play critical roles in light emission, materials stability, and electronic properties.

Herein, we provide a detailed characterization of TPBi's structure and spectrochemical properties, with the end goal of better understanding thin-film morphology (Figure 1). Obtaining new structural data necessitated the growth of single crystals of TPBi; these were generated in a zone furnace via physical vapor transport. The vibrational spectroscopic features were measured with IR and assigned via computational methods, which also unexpectedly identified the conformational variability of TPBi. The combined data allowed for measurement and analysis of molecular orientation in thin films both as-deposited (amorphous) and annealed (crystalline) via IR and X-ray diffraction (XRD) methods.

Received: July 29, 2020 Revised: September 14, 2020

Published: September 17, 2020





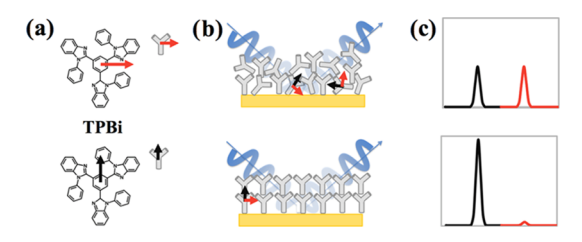


Figure 1. (a) TPBi molecule. The red and black arrows represent two orientations of vibrational modes in the molecules. (b) As-deposited amorphous (top) and annealed crystalline (bottom) TPBi thin films examined via infrared spectroscopy and X-ray diffraction. Ordering within the crystalline film dictates the orientation of vibrations (red and black) relative to surface normal, while in the amorphous film, the vibrations have no preferred orientation. (c) IR modes are observed for which the dipole change vector is perpendicular to the surface and absent for those parallel to the surface. XRD peaks are observed for spacing perpendicular to the surface.

METHODS

Materials. All evaporation metals are of 99.9% or greater purity. Sublimed grade 2,2′,2″-(1,3,5-benzinetriyl)-tris(1-phenyl-1-*H*-benzimidazole) (TPBi) was commercially obtained and used without further purification (>99.5% via HPLC).

Growth of TPBi Crystals. TPBi crystals were grown using a home-built physical vapor transport tube furnace that was 95 cm in length and that had a temperature gradient of approximately \sim 2 °C/cm in the growth zone (Figure S1). One hundred sixteen milligrams of TPBi source material was heated to 310 °C under a flow of ultrahigh purity argon (40 mL/min). The crystals were collected from the region of the furnace at 250–200 °C. Crystals were clear in appearance and less than 2 mm in size.

Single-Crystal X-ray Diffraction Analysis. X-ray diffraction data were obtained from a single crystal mounted on a loop. The data was collected on a Rigaku SuperNova, single-source HyPix3000 diffractometer, with Cu Kα radiation (λ = 1.5406 Å) at 100.01(10) K. Data reduction and absorption correction (multiscan) was performed using the program CrysAlisPro provided by Rigaku. The structures were solved through direct method and refined by full-matrix least-squares methods on F^2 using ShelXT and ShelXL embedded on OLEX2. All nonhydrogen atoms were refined anisotropically, while H atoms were placed in calculated position with their thermal parameters riding in those of their C atoms. Table S1 shows the crystallographic data for TPBi, and Table S2 shows selected bonds and angles.

Preparation of Gold Substrates. Cut microscope slides $(11 \times 25 \times 1 \text{ mm}^3)$ were cleaned in a piranha solution $(3:1, H_2SO_4/H_2O_2)$ for 30 min. The slides were rinsed with copious amounts of 18 M Ω water and 200 proof ethanol, sonicated for 20 min in isopropanol, and dried under a stream of nitrogen. Slides were then mounted in a thermal evaporator (Kurt J. Lesker NANO38). A 5 nm chromium adhesion layer was deposited, followed by 100 nm of gold at a base pressure of <1 \times 10⁻⁶ Torr. Both metals were evaporated at a rate of 1 Å/s.

TPBi Thin-Film Deposition. Freshly prepared gold substrates were added to the sublimation chamber. Upon evacuation to a base pressure 3×10^{-6} Torr, 10-30 nm of TPBi was deposited at a deposition rate of 0.1 or 1 Å/s. After deposition, the substrate was allowed to cool under high vacuum for 30 min.

Annealing of TPBi Thin Films. Under an inert atmosphere, TPBi films were heated to 165 °C for 1 h or 180 °C for 10 min, with the surface temperature monitored via a thermocouple. Samples returned to room temperature over a 30 min period of time.

X-ray Diffraction Analysis of Thin Films. Grazing incidence X-ray diffraction (GIXRD) data were collected with a Bruker D8 Discover 2D fitted with a Co $K\alpha$ source, with an incident angle of 3.6° and 2θ detector angle of 5°. Predicted spectra were generated from crystallographic information using the Mercury software suite from the Cambridge Crystallographic Database Centre. ²³ Samples were prepared on polished silicon wafers rather than microscope slides.

PM-IRRAS Analysis of Thin Films. The molecular orientation of TPBi was assessed via polarization modulation infrared reflection absorption spectroscopy (PM-IRRAS) using a Bruker Optics Tensor 37 FTIR equipped with a PMA 50 accessory and a MCT detector. Thin-film spectra were measured at a resolution of 8 cm⁻¹.

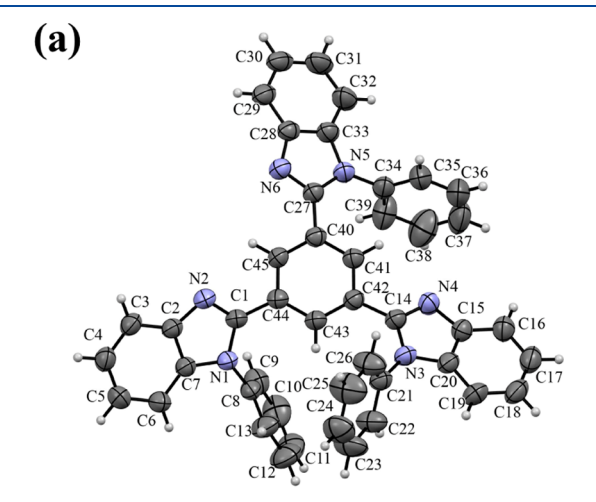
Computational Methods. Quantum mechanical calculations were performed with the Gaussian 16 program, revision B.01.²⁴ The geometry, harmonic vibrational frequency and normal modes, and IR intensities for C_1 , C_3 , and C_{3h} symmetry species of TPBi were calculated using the B3LYP hybrid density functional²⁵ and the 6-31G* basis set. The resulting B3LYP/6-31G* geometry was used for the Møller–Plesset perturbation theory energy calculations with a triple-zeta polarized basis set (MP2/6-311G*).²⁶

RESULTS AND DISCUSSION

X-ray-Based Methodology. Grazing incidence X-ray diffraction is the predominant method for analyzing orientation within thin films.²⁷ Here, the small angle of the incident X-ray beam provides the surface sensitivity, and in polycrystalline or crystalline materials, the phase or preferred orientations are determined from the diffraction peak positions and intensities. There are innumerable examples utilizing GIXRD to determine molecular orientation in organic thin films. In pentacene thin films, GIXRD identified the preferred polymorph generated and the tilt angle of the deposited acene.²⁸ Similar data was acquired for poly(3-hexyl thiophene) under various deposition conditions, 29 various benzothiadiazole copolymers,³⁰ various phthalocyanine composites,³¹ and many others.³² In TPBi films, the lack of structural information has prevented any meaningful analysis of the GIXRD data. 173 Only one crystal structure existed, 16 but it was generated from a solution of methanol, contained solvent molecules within the solved structure, and was not representative of the materials found in thin films and devices. Thus, we grew TPBi single crystals thermally to generate the required structural information.

Crystals of TPBi were grown via physical vapor transport within a home-built zone furnace (Figure S1), commonly utilized for growing organic semiconductors crystals. Growth of the TPBi crystals was complicated by the fact that material preferentially volatilizes from and condenses to a liquid that solidifies with insufficient order to diffract. We found that TPBi could be slowly deposited as crystalline solid by increasing the carrier gas rate to 100 cc/min, which allows a small amount of TPBi to continue past the initial condensation region. Growth via residual vapor meant the process was quite slow (7 days), but it yielded crystals of a quality sufficient for diffraction.

Under these crystal growth conditions, TPBi crystallizes in the orthorhombic space group *Pbca* (Figure 2b). The



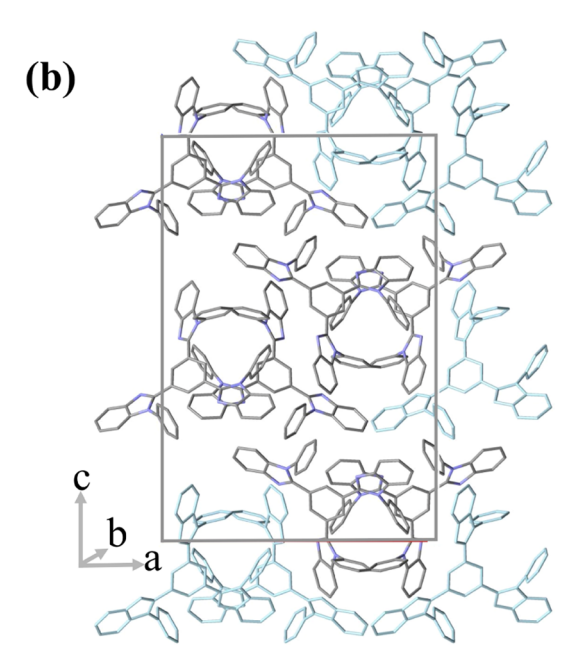


Figure 2. (a) Molecular structure of TPBi with displacement ellipsoids drawn at 50% probability level. (b) Unit cell of TPBi. Cell contains eight TPBi molecules (dark gray), while several adjacent TPBi molecules outside the cell complete the layered structure in the a-b plane, which is used in subsequent thin-film modeling.

dimensions of the unit cell are larger [$\mathbf{a} = 19.3935(2)$ $\mathbf{b} = 12.81750(10)$ $\mathbf{c} = 28.5610(3)$ Å] than for the previous monoclinic $P2_{1/c}$ crystal. Without the methanol solvent molecules in the crystalline lattice, screw axis and glide planes are observed in all three crystallographic axes. Open channels propagate along the \mathbf{b} direction, enabled by the zigzag conformation between pairs of molecules along the \mathbf{a} axis.

In the pure crystal, we observed the disappearance of several inter- and intramolecular interactions and a reduction in the amount of short contacts in the new crystal structure; the previous structure was characterized by having two intramolecular short contacts and several intermolecular ones with the nitrogen atoms from the benzimidazole and the methanol molecule, in addition to those from corners of the phenyl ring with corners of the benzimidazole. The pure crystal structure

of TPBi (Figure 2a) has only one intramolecular short contact between a corner of the central benzene ring and a perpendicularly oriented phenyl ring comprising the atoms C35···H41-C41, with a distance of 2.729 Å. Three corner-to-corner benzimidazole-to-benzimidazole intermolecular short contacts are observed; distances range from 2.75 to 2.89 Å (Figure S2). Phenyl-benzimidazole short contacts between C26-H26···C15 and C26-H26···C16 with distances of 2.859 and 2.865 Å, respectively, consolidate the structure.

Significant differences are also observed on the dihedral angles between the central benzene and the benzimidazole arms, and between these and the phenyl side rings. The solvated structure has dihedral angles between benzene and benzimidazoles of 20.19, 34.57, and 44.59°, and between peripheral phenyl rings and the benzimidazoles of 84.57, 62.71, 51.73°. The pure crystal structure presents an overall reduction on the dihedral angles between benzene and benzimidazoles with 18.70, 23.58, and 39.22° while also exhibiting significant changes in dihedral angles between such and the phenyl side rings, with 69.60, 70.79, and 81.59°. Finally, TPBi molecules are oriented toward the c crystallographic axis, with the central benzene rings tilted 29.18° off this axis. These crystallographic data will allow for the interpretation of the thin-films' GIXRD patterns.

The thin films of TPBi, 10–30 nm thick, were amorphous as first generated, regardless of deposition rate (0.1 or 1 Å/s), or substrate (high-energy gold or low-energy monolayer substrates). However, when samples were annealed at 165 °C for an hour, ¹⁴ visible signs of large mm like domains could be seen under an optical microscope (Figure S3). GIXRD data for annealed films show two distinct peaks at 7.2 and 14.4° (Figure 3a). Diffraction angles were compared with the predicted powder pattern (gray in Figure 3a), which was calculated based on the pure crystal structure. The process reveals the two peaks in the GIXRD pattern to be correlated with (00*l*) planes in the

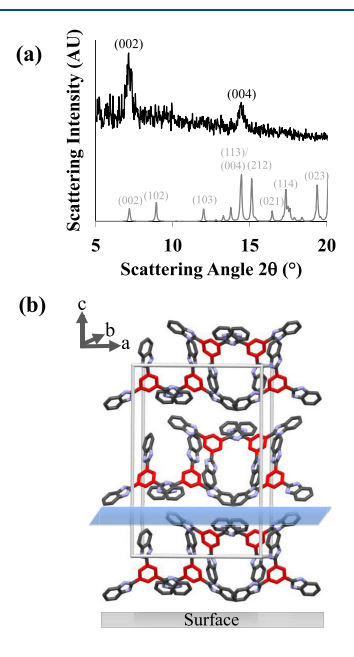


Figure 3. (a) Experimental (black) and calculated (gray) GIXRD pattern of annealed thin-film TPBi. TPBi film thickness is 30 nm. (b) Extended crystal structure, with phenyl substituents omitted, showing orientation and packing. Central benzene rings are highlighted in red. The blue plane corresponds to the (001) plane.

predicted pattern. Specifically, the experimental peak at 7.2° can be unambiguously assigned to the (002) plane, while the (004) plane is the likely assignment for the peak at 14.4° (an overlapping (113) plane prevents this from being entirely unambiguous). Note, that both the (001) and (003) planes are systematically excluded in the powder diffraction via the extinction laws pertaining to the crystal symmetry. This mirrors the experimental data. No other planes are observed in the GIXRD data indicating a significant amount of ordering. As a result, we can be confident that the molecules within the thin film are predominantly oriented with the c crystallographic axis along the surface normal (Figure 3b). In this particular case, the annealed samples show no obvious sign of surface-induced phases (SIP) or polymorphism.³³ The d_{hkl} spacings of 14.25 and 7.12 Å from the GIXRD experiment match those from the unit cell data (14.28 and 7.14 Å for the d(002) and d(004)planes, respectively).

The upright orientation adopted by TPBi, with the (001) plane (a-b face) exposed at the surface (Figure 3b), can be rationalized via intermolecular forces and surface energy considerations.³⁴ To begin, the (001) plane has a much higher reticular density of TPBi molecules than other planes (62 Å²/ molecule for the (001) vs 91 for the (100), for example). 35,36 This in turn generates strong stabilizing intermolecular interactions in the (001) plane, particularly the benzimidazole-benzimidazole and phenyl-benzimidazole short contacts determined from the crystallographic data (Figure 2b). The distance between these rings is consistent with the potential energy minima of the benzene-benzene interaction.³⁷ This is in contrast to the (100) or (010) planes ($\mathbf{b}-\mathbf{c}$ and $\mathbf{a}-\mathbf{c}$ faces) where stabilization is impeded by the presence of the large slip planes between layers (blue in Figure 3b), which prevent meaningful interactions. Thus, an upright configuration maximizes the number of stabilizing interactions over the length of surface. Surface energy is also minimized in this configuration as the surface molecules of the (001) face generate a rather planar configuration in contrast to the corrugated surface generated by TPBi in the (010) plane (Figure S4). The surface generated from the (100) plane also appears destabilized by the dangling benzimidazoles at the surface (Figure 3b, right of figure). Hence, a variety of thermodynamic arguments suggest a very stable surface can be generated at the (001) plane.

IR-Based Methodology. IR analysis of thin film allows the determination of molecular orientation in addition to chemical information.³⁸ If a technique such as infrared reflection absorption spectroscopy is utilized, where the beam reflects off an underlying metallic surface, selection rules arise, which can allow orientation to be assigned.³⁹ Specifically, molecular dipole changes oriented perpendicular to the surface create a reinforcing image dipole in the surface (Figure 1), while those oriented horizontally to the surface generate a negating image dipole. Since IR absorption is proportional to the square of the dipole moment change induced by the given normal vibrational mode, either a stronger absorption band is observed in the former case or no IR absorption in the latter case (Figure 1). This approach has been applied to a wide variety of molecular films.^{28,40}

Without the identity of the various normal vibrational modes, it is impossible to make any assignments and interpret changes in IRRAS data. Thus, quantum mechanical calculations were used to determine the molecular wave function and force constants, and the subsequent harmonic normal

mode analysis yielded frequencies, dipole change vectors, and normal mode vibrations associated with TPBi. The energy minimized molecular structure was in excellent agreement with crystallographic structure, and fidelity between the calculated IR spectra for TPBi and the experimentally determined IR of powder TPBi was good (Figure 4). Normal vibrational mode

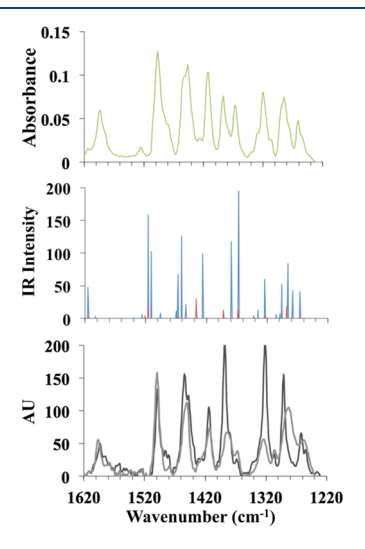


Figure 4. Top: ATR IR spectrum of the powdered TPBi. Middle: Frequencies and intensities (km/mol) of the calculated IR vibrational bands for the C_1 (see crystal structure) and C_3 forms (vide infra) of TPBi are overlaid in blue and red, respectively. The plotted intensities are for a C_1/C_3 ratio of 10:1 that corresponds to the calculated relative free energy of the two conformers of TPBi. Bottom: IRRAS spectrum of 20 nm of TPBi, as deposited at 0.1 Å/s (light gray) and after annealing (dark gray).

assignments were used for the interpretation of IRRAS data for thin films (Figure 4, bottom). Normal modes were described in terms of the prevailing changes in the internal coordinates of TPBi and assigned to the experimental absorption bands (Table 1).

A further note is necessary before discussing the data. During the calculations, a second conformer of TPBi appeared to be of similar energy to the crystallographic form. This conformer possesses a threefold rotational axis (Figure 5) that is perpendicular to the plane of the central phenyl ring and will from here out be referred to as the C_3 conformer. The calculated energy of this C₃ symmetry conformer is 0.95 kcal/ mol higher at the MP2 level of theory than the energy of the C_1 conformer in the gas phase. Thus, the C_3 species is predicted to be roughly 7% of the material in the solid phase when the configurational entropy contribution to the free energy difference is also considered. The calculated IR spectrum for the C_3 conformer is included in both Figure 4 and Table 1; however, in most instances, these bands are not spectroscopically distinct from the dominant C_1 conformer. They do, however, contribute to the overall broadening in the IRRAS spectra and must be considered accordingly.

IRRAS spectra of the thin film were examined for orientation changes after annealing. This approach was limited by the fact that several additional factors are involved in each vibrational band intensity, including the degree of ordering within the solid, conformational equilibria, normal mode degeneracy (Table 1), and the fact that the multitude of functional groups (i.e., the benzimidazole and phenyls) have multiple orientations within the crystal structure. Despite this, the IRRAS does

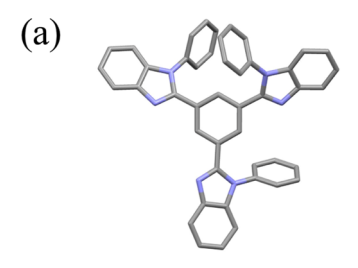
Table 1. Infrared Spectra of TPBi

thin-film frequencies $(cm^{-1})^a$		calculated IR spectra ^b C ₁ symmetry species			calculated IR spectra ^b C ₃ symmetry species			assignments
preanneal	postanneal	freq. $(cm^{-1})^c$	number of modes ^d	int ^e (km/ mol)	freq. (cm ⁻¹) ^c	number of modes ^d	int ^e (km/ mol)	interpretation: Location ^f
596 m	1602 sh	1635	3	6	1635	3	3	ν CC, δ CH: Ph
1578 vw	1593 m	1626	3	40	1625	3	60	ν C-N, ν CC, δ CH: Ph
	1585 sh	1615	5	50	1614	5	48	ν CC, δ CH: Bz, Ph
	1563 vw	1603	3	5	1603	3	2	ν CC, δ CH: Ph
		1539	1	3	1531	1	3	ν CC, ν C=N: Bz, Im
510 sh		1526	1	7	1521	2	59	ν C=N, δ CH: Im, Bz
499 s	1498 s	1516	3	160	1516	3	206	ν C(Ph)-N(Im), ν CC, δ CH: Ph
1499 8	1492 sh	1511	1	104	1310	3	200	ν C=N, ν CC, δ CH: Im, Bz
	1486 w							
1479 w	1481 w	1496	3	10	1496	3	10	δ CH, ν CC: Ph
1/2 **	1471 vw	1470	3	13	1469	3	8	δ CH, ν CC: Ph
156 ch	1454 s	1467	2	69	1466	2	62	δ CH, ν C=N, ν CC: BIm, Bz
1456 sh 1450 s			1			1	16	
430 8	1448 s	1461		128	1463	1	10	δ CH, ν C=N, ν CC: BIm, Bz
	1439 sh	1454	1	233				δ CH, ν CC, ν C=N: BIm C ₃ , Bz (TPBi C ₁
413 m	1414 m	1426	1	101	1437	2	317	δ CH, ν CC, ν C=N: BIm, Bz
385 m	1389 s	1379	2	120	1392	1	144	ν C=N, ν CC, δ CH: Im, Bz
377 sh	1377 sh	1367	4	197	1368	5	161	ν C-N, ν C=N, ν CC, δ CH: BIm,
1367 w	1368 vw							,
	1341 vw	1342	1	6	1345	1	2	ν CC, ν C=N, δ CH: Bz, Im
330 sh	1330 sh	1335	4	15	1336	4	6	δ CH: Ph
324 m	1322 s	1324	2	62	1323	2	62	δ CH, ν C=N: BIm, Ph
132 111	-5	1312	1	0.1	1312	1	1	δCH: Bz, Ph
306 w	1308 vw	1305	2	8	1304	3	4	δCH: BIm, Ph
1300 W	1300 / 11	1299	1	9	1301	3	•	δCH: BIm, Bz
		1296	1	54				ν C-N, ν C=N, δ CH: Im, Bz
282 s,br	1291 s	1286	1	86	1288	3	201	ν C-N, ν C=N, δ CH: BIm
202 8,01	1291 8	1278	2			1	1	
258 m,br	1262 m 1254 w	1266	2	45 43	1275 1266	2	36	ν C-N, ν C=N, δ CH: BIm, Bz ν CC, ν C-N, δ CH: BIm
1195 vw	1195 vw	1199	3	42	1200	3	42	ν C-N, δ CH: BIm, Ph
-,0	,0	1183	3	2	1182	3	1	δ CH: Ph
		1170	3	0.1	1170	3	0.1	δCH: Ph
	1150 vw	1160	3	3	1160	3	3	δCH: BIm
	1130 vw	1138	1	2	1100	3	3	ν CC, δ CH: Bz, BIm
120 1	1115 w				1122	2	7	
1120 w,br	1115 W	1128	2	5	1132	3	7	ν CC, δ CH: Bz, BIm
	4.0=0	1118	3	0.4	1118	3	0.2	δCH: Ph
1075 w	1070 w	1087	3	13	1087	3	12	δCH: <i>Ph</i>
	1048 vw					_		ν CC, δ CH: Bz, BIm
	1032 vw	1039	3	5	1038	3	5	δCH: Ph
013 w	1016 m	1020	3	38	1020	3	50	δ CH, ν CC: BIm
998 vw	1000 vw	1000	3	4	1000	3	4	δ6R: Ph
		996	3	9	996	3	11	δ SR, δ 6R, ν CC: Im, Bz, Ph
	970 w	975	4	5	979	4	7	δ 5R, δ 6R, ν CC, γ CH: Im, Ph
		951 937	6 1	0.7 1	952	6	0.8	γCH: BIm, Ph γCH: Bz
36 w	936 w	931	2	21	932	2	23	γCH: Ph
		917	2	6	924	3	1	γCH: Ph
07 vw,br	906 w	914	3	5	914	3	4	γCH: Ph
707 VW,01			-		908	1	8	γCH: Ph
		902	3	4	903	2	1	γCH: Ph
91 w	890 w	894	1	21	896	1	15	δ5R, δ6R: BIm
77 sh	877 w	879	1	17		-	-	δ6R, δ5R: Bz, BIm
	874 w	877	1	33	878	2	53	δ6R, δ5R: Bz, BIm
875 w	J		3	1	849	3	1	γCH: BIm
/5 W	848 ww	X49						
/5 W	848 vw	849 836						•
/5 W	848 vw 835 vw	849 836 819	3	1 3	836 820	3	1	γ CH: Ph breathing mode: Bz , BIm

Table 1. continued

thin-film frequencies $(cm^{-1})^a$		calculated IR spectra b C_1 symmetry species			calculated IR spectra C3 symmetry species			assignments
preanneal	postanneal	freq. $(cm^{-1})^c$	number of modes ^d	int ^e (km/ mol)	freq. $(cm^{-1})^c$	number of modes ^d	int ^e (km/ mol)	interpretation: Location ^f
764 m	764 s	760	4	41	759	3	51	γCH (in-phase): BIm, Ph
	755 s	744	3	78	744	3	91	γCH (in-phase): BIm
744 m,br	749 s	741	2	67	740	2	35	γ CH, δ 6R, δ 5R: $TPBi$
		728	1	3	728	1	2	γ5R, γCH: BIm, Ph
715 sh,vw	713 sh,w	719	1	0.1	719	2	25	γ5R, γCH: BIm, Ph
		712	1	4				δ 5R, δ 6R: $TPBi$
705 w	708 m	708	2	37	707	1	8	γ6R, γ5R: TPBi
		703	1	15	705	2	44	$\delta 6 R$, $\delta 5 R$: $TPBi$
696 m	695 s	695	3	82	696	3	67	γ6R: Ph
680 sh	680 w	685	1	13	689	1	6	γ6R, γ5R: Bz, Im
672 vw	669 sh	652	1	12				δ 6R5R linkage, δ 6R, δ R6: Bz, BIm, P
					639	1	1	δ6R5Rlinkage, δ6R: Bz, BIm
660 vw	662 w	631	1	12	627	2	54	δ6R5Rlinkage, δ6R, γ6R: Bz, BIm, Ph
		622	3	9	620	3	4	δ6R: Ph
		618	3	5	616	3	2	δ6R, δ5R: BIm, Ph
		610	1	21				δ6R, δ5R: BIm, Ph

^aStrong (s), medium (m), weak (w), very (v), and shoulder (sh). ^bB3LYP/6-31G* method, 4 cm⁻¹ resolution. ^cScaled B3LYP/6-31G* frequencies (0.98 scale factor was used). ^dNormal modes separated by less than 4 cm⁻¹ were considered to constitute a single spectral band. The number of normal modes contributing to this band is given. ^eTotal intensity of all normal modes contributing to a spectral band. ^fν, δ, and γ denote bond stretching, angle bending (in-plane), and dihedral angle bending, respectively. 5R and 6R denote vibrations delocalized over the entire five- and six-membered rings, respectively. BIm = benzimidazole; Ph = phenyl (substituent); and Im = imidazole; Bz = benzene (core).



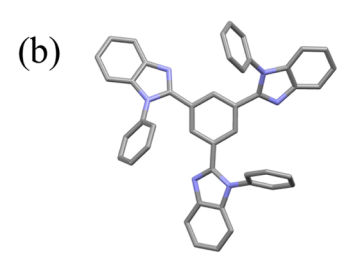


Figure 5. Stick structure calculated of the C_1 (a) and C_3 (b) conformers of TPBi.

allow us to confirm the orientation determined by GIXRD. To do so, we have selected several lines (1596, 705, 696 cm⁻¹) where the contributions from each conformer are roughly the same and where the full width half-max is comparable such that orientation-based intensity changes can be isolated. As can be seen in Figure 6, the higher wavenumber feature has a small decrease, while the vibrations near 700 cm⁻¹ both increase significantly. Analysis of the bands at 1596 and 696 cm⁻¹ are the most straightforward. The absorption at 1596 cm⁻¹ corresponds to CC vibrations and in-plane C–H bends of the phenyl group, while the 696 cm⁻¹ bands correspond to out-of-plane bends on the same phenyl substituents. It thus makes sense that these two intensities would change counter to each other. The intensity changes can qualitatively be justified

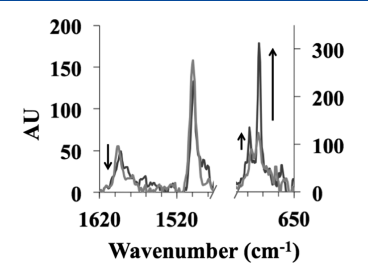


Figure 6. Selected regions of the IRRAS spectrum of 20 nm of TPBi as deposited at 0.1 Å/s on top of a freshly prepared gold surface (light gray) and after annealing (dark gray). Note, the y-axis values differ for the two segments.

by orientation information in the GIXRD data as well. In TPBi, the central benzene rings are most aligned with the surface normal (29°) after annealing. Unsurprisingly, significant planar modes associated with this group (1454, 1450, 1413, 1385, 1282 cm⁻¹, Figure S5) exhibit significant increases in intensity. Thus, IR measurements are nominally consistent with GIXRD results.

The combined IR and XRD data has several implications, some of which were unexpected. To begin, the presence of the clear slip planes within the single-crystal unit cell suggests that there should be a strong preference for TPBi to orient with $\mathbf{a}-\mathbf{b}$ crystallographic face exposed (in contrast to the structure from solution grown crystals). This is in contrast with known deposition characteristics, namely that TPBi deposits as an amorphous thin film and remains so unless annealed. While this can be attributed to the inefficient packing caused by TPBi molecular structure (and the small lattice energy), it is likely that the presence of the second TPBi conformer inhibits unassisted formation of an ordered structure. It is well known that crystallization of TPBi thin films is readily inhibited by small amounts of other organic semiconductors; thus, it seems likely that here the C_3 conformer acts in a similar

function. With the structure of these materials known, film structure determined, and a complicating factor in the C_3 conformer identified, it now becomes possible to improve fabricated optoelectronic devices and the theoretical models, which underpin device behavior. Finally, the measured orientation has large implications for the amorphous thin films of TPBi. It is known that disordered films of TPBi also have a preferred orientation which generates spontaneous orientation polarization, which impacts interfacial charge accumulation, in turn quenching excitons in OLEDs. Un measurement suggests the preferred orientation for amorphous films, a critical variable in surface potential models used to interpret these interfacial structures.

CONCLUSIONS

In summary, we have characterized the structural properties of TPBi critical to understanding its thin film material behavior. The limited intermolecular interactions dictating a thin-film structure were identified via single-crystal X-ray diffraction data. Additionally, unit cell and symmetry data (in conjunction with GIXRD measurements) demonstrate that annealed TPBi thin films preferentially orient with the a-b crystallographic face parallel to the substrate and with the central benzene rings oriented 29° from the surface normal. This orientation can be understood based on molecular packing within the crystal, which shows obvious slip planes in the direction of the thinfilm's surface. IRRAS measurements are in agreement with this assignment. Computational structural analysis suggests that there is an additional C_3 conformer, which may be the source of TPBi's amorphous film stability. These results make it possible for academic and industrial OLED researchers to optimize this electron transport layer's material properties.

ASSOCIATED CONTENT

Supporting Information

The Supporting Information is available free of charge at https://pubs.acs.org/doi/10.1021/acs.jpcc.0c06959.

Crystal growth furnace photos and temperature profile; packing diagram indicating short contacts; magnified images of the annealed TPBi film; unit cell for TPBi viewed along the a axis; full IRRAS spectrum of thin-film TPBi before and after annealing; tabular crystallographic data and selected bonds and angles; B3LYP/6-31G* optimized Cartesian coordinates (pdb format) of the C_1 and C_3 conformers of TPBi (PDF)

AUTHOR INFORMATION

Corresponding Author

Jacob W. Ciszek — Department of Chemistry and Biochemistry, Loyola University Chicago, Chicago, Illinois 60660, United States; orcid.org/0000-0002-6860-2900; Email: jciszek@luc.edu

Authors

Jazmin Calimano – Department of Chemistry and Biochemistry, Loyola University Chicago, Chicago, Illinois 60660, United States

Feifei Li — Department of Chemistry and Biochemistry, Loyola University Chicago, Chicago, Illinois 60660, United States Jan Florian — Department of Chemistry and Biochemistry, Loyola University Chicago, Chicago, Illinois 60660, United States; orcid.org/0000-0003-2669-4293

- Dalice M. Piñero-Cruz Department of Chemistry and the Molecular Sciences Research Center, University of Puerto Rico, San Juan, Puerto Rico 00931, United States
- Thomas R. Fielitz Department of Chemical Engineering and Materials Science, University of Minnesota, Minneapolis, Minnesota 55455, United States
- Russell J. Holmes Department of Chemical Engineering and Materials Science, University of Minnesota, Minneapolis, Minnesota 55455, United States; orcid.org/0000-0001-7183-3673

Complete contact information is available at: https://pubs.acs.org/10.1021/acs.jpcc.0c06959

Notes

The authors declare no competing financial interest.

ACKNOWLEDGMENTS

The single-crystal X-ray diffractometer was acquired through the support of the National Science Foundation (NSF) under the Major Research Instrumentation Award Number CHE-1626103. J.W.C. thanks a Loyola University Chicago research support grant for materials. R.J.H. and T.R.F. acknowledge support from the NSF Solid-State and Materials Chemistry Program under DMR-1307066.

REFERENCES

- (1) OLED Fundamentals: Materials, Devices, and Processing of Organic Light-Emitting Diodes, 1st ed.; Gaspar, D. J.; Polikarpov, E., Eds.; CRC Press: Boca Raton, FL, 2015.
- (2) Zhou, H.; Chen, Q.; Li, G.; Luo, S.; Song, T.; Duan, H.-S.; Hong, Z.; You, J.; Liu, Y.; Yang, Y. Interface Engineering of Highly Efficient Perovskite Solar Cells. *Science* **2014**, *345*, 542–546.
- (3) Kulkarni, A. P.; Tonzola, C. J.; Babel, A.; Jenekhe, S. A. Electron Transport Materials for Organic Light-Emitting Diodes. *Chem. Mater.* **2004**, *16*, 4556–4573.
- (4) Gao, Z.; Lee, C. S.; Bello, I.; Lee, S. T.; Chen, R.-M.; Luh, T.-Y.; Shi, J.; Tang, C. W. Bright-Blue Electroluminescence from a Silyl-Substituted Ter-(Phenylene–Vinylene) Derivative. *Appl. Phys. Lett.* **1999**, *74*, 865–867.
- (5) Tao, Y.; Yang, C.; Qin, J. Organic Host Materials for Phosphorescent Organic Light-Emitting Diodes. *Chem. Soc. Rev.* **2011**, *40*, 2943–2970.
- (6) Tsuji, H.; Sato, K.; Sato, Y.; Nakamura, E. Benzophosphole Oxide and Sulfide for Thermally Stable Cathode Buffer Layers in Organic Thin-Film Photovoltaic Devices. *Chem. Asian J.* **2010**, *5*, 1294–1297.
- (7) Turak, A. Interfacial Degradation in Organic Optoelectronics. RSC Adv. 2013, 3, 6188–6225.
- (8) Yu, J.; Wang, N.; Zang, Y.; Jiang, Y. Organic Photovoltaic Cells Based on TPBi as a Cathode Buffer Layer. *Sol. Energy Mater. Sol. Cells* **2011**, 95, 664–668.
- (9) Jang, J. G.; Shin, H. K. High Efficiency Green Phosphorescent Organic Light Emitting Device with (TCTA/TCTA0.5TPBi0.5/TPBi): Ir(Ppy)3 Emission Layer. *Thin Solid Films* **2009**, *517*, 4122–4126.
- (10) Lo, S.-C.; Male, N. A. H.; Markham, J. P. J.; Magennis, S. W.; Burn, P. L.; Salata, O. V.; Samuel, I. D. W. Green Phosphorescent Dendrimer for Light-Emitting Diodes. *Adv. Mater.* **2002**, *14*, 975–979
- (11) Cheng, L. F.; Hung, L. M.; Ding, X. M.; Gao, Z. Q.; Lee, C. S.; Lee, S. T. Photoemission Study of a New Electroluminescent Material: Trimer of N-Arylbenzimidazoles (TPBI). *Displays* **2000**, *21*, 51–54.
- (12) Li, Y. Q.; Fung, M. K.; Xie, Z.; Lee, S.-T.; Hung, L.-S.; Shi, J. An Efficient Pure Blue Organic Light-Emitting Device with Low Driving Voltages. *Adv. Mater.* **2002**, *14*, 1317–1321.

- (13) Kan, W.; Zhu, L.; Wei, Y.; Ma, D.; Sun, M.; Wu, Z.; Huang, W.; Xu, H. Phosphine Oxide-Jointed Electron Transporters for the Reduction of Interfacial Quenching in Highly Efficient Blue PHOLEDs. J. Mater. Chem. C 2015, 3, 5430–5439.
- (14) Bangsund, J. S.; Fielitz, T. R.; Steiner, T. J.; Shi, K.; Van Sambeek, J. R.; Clark, C. P.; Holmes, R. J. Formation of Aligned Periodic Patterns during the Crystallization of Organic Semiconductor Thin Films. *Nat. Mater.* **2019**, *18*, 725–731.
- (15) Gong, J.-R.; Wan, L.-J.; Lei, S.-B.; Bai, C.-L.; Zhang, X.-H.; Lee, S.-T. Direct Evidence of Molecular Aggregation and Degradation Mechanism of Organic Light-Emitting Diodes under Joule Heating: An STM and Photoluminescence Study. *J. Phys. Chem. B* **2005**, *109*, 1675–1682.
- (16) Song, W.-F.; Wu, Y.; Fan, Y.; Wang, Y.; Liu, Y. 1,3,5-Tris(N-Phenylbenzimidazol-2-Yl)Benzene Methanol Solvate. *Acta Crystallogr., Sect. E: Struct. Rep. Online* **2009**, *65*, No. 02461.
- (17) Fielitz, T. R.; Phenicie, C. M.; Holmes, R. J. Effects of Additives on Crystallization in Thin Organic Films. *Cryst. Growth Des.* **2017**, *17*, 4522–4526.
- (18) Fielitz, T. Understanding and Engineering Molecular Order in Organic Semiconductors. Ph.D. Dissertation, University of Minnesota, Minneapolis, MN, 2017.
- (19) CrysAlis PRO. Rigaku Oxford Diffraction: Wroclaw, Poland, 2016.
- (20) Dolomanov, O. V.; Bourhis, L. J.; Gildea, R. J.; Howard, J. A. K.; Puschmann, H. *OLEX2*: A complete structure solution, refinement and analysis program. *J. Appl. Crystallogr.* **2009**, 42, 339–341.
- (21) Sheldrick, G. M. SHELXT Integrated space-group and crystal-structure determination. Acta Crystallogr., Sect. A: Found. Adv. 2015, 71. 3–8.
- (22) Sheldrick, G. M. Crystal structure refinement with SHELXL. Acta Crystallogr., Sect. C: Struct. Chem. 2015, 71, 3–8.
- (23) Macrae, C. F.; Bruno, I. J.; Chisholm, J. A.; Edgington, P. R.; McCabe, P.; Pidcock, E.; Rodriguez-Monge, L.; Taylor, R.; van de Streek, J.; Wood, P. A. *Mercury CSD 2.0* new features for the visualization and investigation of crystal structures. *J. Appl. Crystallogr.* **2008**, *41*, 466–470.
- (24) Frisch, M. J.; Trucks, G. W.; Schlegel, H. B.; Scuseria, G. E.; Robb, M. A.; Cheeseman, J. R.; Scalmani, G.; Barone, V.; Petersson, G. A.; Nakatsuji, H. et al. *Gaussian 16*, Revision B.01; Gaussian, Inc.: Wallingford, CT, 2016.
- (25) Becke, A. D. Density-functional Thermochemistry. III. The Role of Exact Exchange. *J. Chem. Phys.* **1993**, *98*, 5648–5652.
- (26) Hehre, W. J.; Radom, L.; Schleyer, P.; von, R.; Pople, J. *Ab Initio Molecular Orbital Theory*, 1st ed.; Wiley-Interscience: New York, 1986.
- (27) Feidenhans'l, R. Surface Structure Determination by X-Ray Diffraction. Surf. Sci. Rep. 1989, 10, 105–188.
- (28) Hu, W. S.; Tao, Y. T.; Hsu, Y. J.; Wei, D. H.; Wu, Y. S. Molecular Orientation of Evaporated Pentacene Films on Gold: Alignment Effect of Self-Assembled Monolayer. *Langmuir* **2005**, *21*, 2260–2266.
- (29) Yang, H.; LeFevre, S. W.; Ryu, C. Y.; Bao, Z. Solubility-Driven Thin Film Structures of Regioregular Poly(3-Hexyl Thiophene) Using Volatile Solvents. *Appl. Phys. Lett.* **2007**, *90*, No. 172116.
- (30) Sirringhaus, H. 25th Anniversary Article: Organic Field-Effect Transistors: The Path Beyond Amorphous Silicon. *Adv. Mater.* **2014**, 26, 1319–1335.
- (31) Xu, Z.-X.; L. Roy, V. A.; Low, K.-H.; Che, C.-M. Bulk Heterojunction Photovoltaic Cells Based on Tetra-Methyl Substituted Copper(II) Phthalocyanine:P3HT:PCBM Composite. *Chem. Commun.* **2011**, 47, 9654–9656.
- (32) Wen, Y.; Liu, Y.; Guo, Y.; Yu, G.; Hu, W. Experimental Techniques for the Fabrication and Characterization of Organic Thin Films for Field-Effect Transistors. *Chem. Rev.* **2011**, *111*, 3358–3406.
- (33) Winokur, M. J.; Huss-Hansen, M. K.; Lauritzen, A. E.; Torkkeli, M.; Kjelstrup-Hansen, J.; Knaapila, M. Modeling of Grazing-Incidence X-Ray Diffraction from Naphthyl End-Capped Oligothiophenes in

- Organic Field-Effect Transistors. Cryst. Growth Des. 2020, 20, 3968–3978
- (34) Witte, G.; Wöll, C. Growth of Aromatic Molecules on Solid Substrates for Applications in Organic Electronics. *J. Mater. Res.* **2004**, *19*, 1889–1916.
- (35) Wells, A. F. XXV. Crystal Habit and Internal Structure.—II. London, Edinburgh Dublin Philos. Mag. J. Sci. 1946, 37, 217–236.
- (36) Winn, D.; Doherty, M. F. A New Technique for Predicting the Shape of Solution-Grown Organic Crystals. *AIChE J.* **1998**, *44*, 2501–2514.
- (37) Jorgensen, W. L.; Severance, D. L. Aromatic-Aromatic Interactions: Free Energy Profiles for the Benzene Dimer in Water, Chloroform, and Liquid Benzene. *J. Am. Chem. Soc.* **1990**, *112*, 4768–4774.
- (38) Li, F.; Hopwood, J. P.; Galey, M. M.; Sanchez, L. M.; Ciszek, J. W. Chemically Transformed Monolayers on Acene Thin Films for Improved Metal/Organic Interfaces. *Chem. Commun.* **2019**, *55*, 13975–13978.
- (39) Griffiths, P. R.; Haseth, J. A. D.; Winefordner, J. D. Fourier Transform Infrared Spectrometry, 2nd ed.; Wiley-Interscience: Hoboken, NJ, 2007.
- (40) Deye, G. J.; Vicente, J. R.; Chen, J.; Ciszek, J. W. Influence of Defects on the Reactivity of Organic Surfaces. *J. Phys. Chem. C* **2018**, 122, 15582–15587.
- (41) Liu, Z.-Y.; Tseng, S.-R.; Chao, Y.-C.; Chen, C.-Y.; Meng, H.-F.; Horng, S.-F.; Wu, Y.-H.; Chen, S.-H. Solution-Processed Small Molecular Electron Transport Layer for Multilayer Polymer Light-Emitting Diodes. *Synth. Met.* **2011**, *161*, 426–430.
- (42) Osada, K.; Goushi, K.; Kaji, H.; Adachi, C.; Ishii, H.; Noguchi, Y. Observation of Spontaneous Orientation Polarization in Evaporated Films of Organic Light-Emitting Diode Materials. *Org. Electron.* **2018**, *58*, 313–317.
- (43) Noguchi, Y.; Miyazaki, Y.; Tanaka, Y.; Sato, N.; Nakayama, Y.; Schmidt, T. D.; Brütting, W.; Ishii, H. Charge Accumulation at Organic Semiconductor Interfaces Due to a Permanent Dipole Moment and Its Orientational Order in Bilayer Devices. *J. Appl. Phys.* **2012**, *111*, No. 114508.
- (44) Bangsund, J.; Van Sambeek, J. R.; Holmes, R. J. Sub-Turn-on Exciton Quenching due to Molecular Orientation and Polarization in Organic Light-Emitting Devices. *Sci. Adv.* **2020**, *6*, eabb2659.